Int. J. Electrochem. Sci., 8 **(2013)** 12780 - 12800

International Journal of
ELECTROCHEMICAL
SCIENCE
www.electrochemsci.org

Comparison of TiO_2 and TiO_2-CNT as Cathode Catalyst Supports for ORR

C. Montero-Ocampo[1*], *J.R. Vargas Garcia*[2], *E. Arce Estrada*[2]

[1]CINVESTAV-IPN, U. Saltillo, Apartado Postal 663, 25900 Ramos Arizpe, Coahuila, México
[2]Dpto. Ing. en Metalurgia y Materiales, ESIQIE-IPN, UPALM, Zacatenco, 07738 México D.F.
[*]E-mail: cecilia.montero@cinvestav.edu.mx

Received: 31 July 2013 / *Accepted:* 10 September 2013 / *Published:* 20 October 2013

The aim of the present study is to compare the properties of Pt-TiO_2, where TiO_2 is utilized as a catalyst support, with those obtained from Pt-TiO_2-CNT synthesized using MOCVD. The results showed that the Pt-TiO_2-CNT composites displayed higher Pt activity than the Pt-TiO_2 catalysts. X-ray diffraction studies revealed that both Pt-TiO_2 and Pt-TiO_2-CNT exhibited a body-centered tetragonal anatase TiO_2 crystal structure. However, when fragmentation of the raw materials was vigorous, the particle size became smaller and the synthesized Pt-TiO_2-CNT composites displayed an amorphous structure with lower intensity TiO_2 reflections. STEM micrographs of the composites showed well-dispersed Pt nanoparticles deposited on anatase agglomerates and/or on CNT supports. Nevertheless, the Pt particles on TiO_2 aggregates are electronically isolated, resulting in the performance of the electrodes being limited by insufficient local electronic conductivity and the low bulk electronic conductivity of TiO_2. The carbon nanotubes in the Pt-TiO_2-CNT composites create an electron-conducting network, resulting in an increase in macroscopic electronic conductivity. Comparisons of the Pt activity towards the O_2 reduction reaction (ORR) indicate that the Pt-TiO_2-CNT catalysts possess better performance, regardless of CNT percentage, than the Pt-TiO_2 composites. The overall ORR performance is enhanced with an increased percentage of CNT, mainly due to the relatively high conductivity of the CNT support. In contrast, the CNT-free Pt-TiO_2 cathode had lower oxygen reduction activity due to the limited electronic conductivity of TiO_2. This study demonstrates a stable Pt-TiO_2-CNT composite material possessing a performance comparable to the conventional Pt-CNT material.

Keywords: Titanium oxide, Carbon Nanotubes, Oxygen reduction reaction

1. INTRODUCTION

Many previous works have focused on the use of Pt-based electrocatalysts in both hydrogen evolution reactions (HER) and oxygen reduction reactions (ORR). The uniformity of distribution of Pt

on the support (generally carbon powder), the catalyst porosity and the nanoparticle size are the primary factors reported as important for the stability and high efficiency of proton exchange membrane fuel cells (PEMFC). Considerable research has been conducted toward the development of new electrocatalysts with various compositions that show high catalytic activity of platinum on carbon powder. However, degradation of the catalyst support material in the gas diffusion electrode (GDE) of a PEMFC is caused by the corrosion of the catalyst-supporting carbon in the cathodic PEMFC environment, which includes high acidity, electrochemical potential, water, and O_2 [1]. Carbon corrosion ($C + 2H_2O \rightarrow CO_2 + 4H^+ + 4e^-$), which occurs at potentials higher than 0.207 V/RHE [2], is a severe problem that compromises fuel cell durability. This corrosion results in decreased contact between the support and the Pt catalyst particles, which consequently become more mobile and either aggregate into larger Pt particles or migrate out of the GDE. Degradation of the carbon support also results in a significant loss of active catalyst area [3]. Therefore, alternative support materials are urgently sought to provide both the required electronic conductivity and electrochemical stability.

The development of more stable carbon supports, such as those utilizing graphitized carbon, is one current approach to stabilize the supports and eliminate carbon corrosion [4]. Alternative support materials (i.e., conductive ceramics, such as titanium, tungsten and zirconium oxides) with dimensions in the nanometer range have also been proposed [5, 6]. Among these, TiO_2 is a particularly interesting catalyst support material due to its excellent mechanical and chemical stability at PEMFC cathodic potentials in acidic aqueous environments [7-13]. It has been reported that TiO_2 prevents the agglomeration of Pt particles and effectively disperses Pt atoms in clusters [7, 14]. Additionally, TiO_2 supports control the nanostructure of the catalyst and provide both thermal and oxidative stability. Experimentally, a TiO_2-supported catalyst showed similar performance to carbon-supported Pt in a H_2 PEM fuel cell operated at 60 °C and 0.8 V [14]. However, application of the ceramic support yielded lower performance in the ohmic regime due to its higher electrical resistance [14]. Other studies found that TiO_2 improves Pt oxygen reduction activity by facilitating mechanisms such as reactant surface diffusion and oxygen spill-over [14].

Pt nanoparticles have been supported on TiO_2 surfaces using different methods. TiO_2 nanoparticles have been synthesized using the sol–gel method and platinized [14]. An electrospinning method has been used to grow titania nanofibers decorated with Pt [15]. A homogeneous dispersion of Pt nanoparticles on a TiO_2 surface has been achieved by $NaBH_4$ reduction in an ethylene glycol-based solution [16]. Pt was deposited onto TiO_2 nanotubes through either sputtering or evaporation [17]. The sputtered catalyst outperformed the Pt obtained by evaporation, which was indicated by a favorable shift of the ORR onset potential [17]. It has been reported that Pt dispersed on mesoporous TiO_2 showed similar performance to a carbon-supported Pt catalyst [18]. Kraemer [1], in a thermal stability study evaluating anatase as a catalyst support material in Pt-TiO_2-C composite gas diffusion electrodes, found high carbon stability that was likely due to the reduced direct contact between Pt and C, as Pt nanoparticles were supported predominantly on TiO_2. This study demonstrated a stable Pt-TiO_2-C composite material with comparable performance to conventional Pt-C materials.

In the present work, a metal-organic chemical vapor deposition (MOCVD) process was employed for the deposition of catalytic Pt centers on TiO_2 to produce Pt-TiO_2 (PT) catalysts. Anatase was investigated as the Pt support in the Pt-TiO_2 composites. Pt-TiO_2-CNT catalysts (referred to as

PTN) were also prepared, incorporating carbon nanotubes (CNT) as an electron-conducting component to compensate for the low electronic conductivity of TiO_2. CNTs, with their graphitic structure, are more electrochemically stable than Vulcan XC-72 and show a lower susceptibility to corrosion [3]. A catalyst without TiO_2, Pt-CNT (referred to as PNT), was prepared as a reference.

The effects of support modification with TiO_2 and/or CNTs on the electrochemical stability and oxygen reduction performance were investigated. The structures of the prepared composites were investigated using X-ray diffraction (XRD). The physical morphologies of the composites were examined using field emission scanning electron microscopy (FESEM) and scanning transmission electron microscopy (STEM), while their elemental compositions were determined using energy-dispersive X-ray spectroscopy (EDS). Their electrochemical stability was studied using cyclic voltammetry (CV) and their oxygen reduction activity using linear voltammetry (LV).

2. EXPERIMENTAL PART

Electrocatalysts were synthesized by MOCVD from raw materials. Carbon nanotubes (CNT, referred to in the figures as N) were mixed homogeneously with TiO_2 nanoparticles (referred to in the figures as T) and a sublimable organoplatinum solid, Pt(II) acetylacetonate ($[C_5H_7O_2]_2Pt$, Aldrich, referred to in the figures as P), as the Pt source. Such mixtures were ground in an agate mortar. The sufficiently high vapor pressure and sufficiently low sublimation (170 °C) and decomposition temperatures allowed rapid material transport of the Pt source material. The organic content of the Pt source acted as reducing agent for the metal ion, enabling the deposition of the Pt particles on the support. The ligands were oxidized and decomposed to nonvolatile carbon residues on the catalyst-support, and all volatile by-products were removed by a flow of argon gas through the reaction chamber.

Pt-TiO_2 catalysts with Pt fractions of 1 *at%* (PT10), 2 *at%* (PT15) and 3 *at%* (PT20) were prepared by adding the calculated amount of platinum acetylacetonate $[C_5H_7O_2]_2Pt$ (Aldrich) to the calculated amount of titanium (IV) oxide nanopowder (Aldrich), and the whole was fragmented and mixed together. Similarly, the Pt-TiO_2-CNT catalysts with 33 *vol%* CNT (PTN33), 50 *vol%* CNT (PTN50) and 67 *vol%* CNT (PTN67) were prepared by adding the calculated amount of platinum organometallic to the calculated amounts of titanium (IV) oxide nanopowder and carbon nanotubes. For PTN33 and PTN67, all the reagents were mixed together without fragmentation; however, for PTN50 the reagents were mixed together and fragmented in an agate mortar for 30 min before synthesis to examine the effect of fragmentation. The same procedure used for PTN50 was repeated for the Pt-CNT (PNT) composite with 99.96 *vol%* CNT.

The prepared catalysts were each loaded onto a quartz carrier, positioned horizontally in the first zone of a three-zone reaction furnace, and then heated at 200 °C for 10 min to remove ligands and reduce metal particles. The quartz carrier was then moved to the next zone of the reaction furnace and heated at 450 °C for 10 min, all over which the furnace was evacuated and purged with an argon gas flow (100 sccm). To prevent condensation of the sublimable source material, all surfaces of the reactor

outside of the reaction zone were maintained at temperatures greater than the source sublimation temperature.

Structures of the catalyst composites, the as-received TiO_2, and the carbon nanotubes were determined by X-ray diffraction (XRD) using a D8 Focus Bruker AXS X-ray diffractometer equipped with a Cu-K_α radiation source (λ= 1.54056 Å) operated at 35 KV and 25 mA. The 2θ angle intervals were analyzed from 20^o to 90^o at a scan rate of 4^o/min. Composite morphologies were examined by field emission scanning microscopy (FESEM) and scanning transmission electron microscopy (STEM). The elemental compositions of the material surfaces were obtained by EDS.

A three-electrode cell was used for electrochemical characterization. The working electrode was a 5 mm glassy carbon rotating disk (RDE) (0.19635 cm^2 exposed geometric area) onto which the catalytic ink was deposited. A large area glassy carbon electrode was used as counter electrode. A mercury-mercurous sulfate (Hg/Hg_2SO_4, K_2SO_4 sat) MSE electrode was used as a reference electrode; however, all reported potentials were referenced to the hydrogen reference electrode (HRE).

The catalytic ink was prepared by dispersing 5 mg of prepared Pt-TiO_2, Pt-TiO_2-CNT or Pt-CNT powder in 300 µL of chromatographic-grade ethanol containing 10 µL of an ionically conductive polymer electrolyte (Nafion). In each case, the slurry was subjected to ultrasonic agitation for 20 min until all small grains disappeared. Finally, 5 µL of prepared ink was placed on the RDE surface and allowed to dry in a vacuum desiccator for 24 h.

Cyclic voltammetry (CV) experiments were conducted in a 0.5 M H_2SO_4 electrolyte solution at room temperature. Prior to the experiment, the electrolyte was purged with nitrogen gas for approximately 20 min to remove any dissolved oxygen. CV curves were recorded for the RDE coated with a catalyst layer after scanning for 1, 25 and 50 cycles (to obtain stable voltammogram curves) in the potential range from 1.28 V to -0.10 V for PT composites, and from 1.13 V to 0.00 V for PTN catalysts, at a scan rate of 50 mVs^{-1}. Current densities are reported per mg of Pt used.

Linear voltammetric oxygen reduction experiments were conducted using an O_2-saturated 0.5 M H_2SO_4 electrolyte with a decreasing potential trend from 1.0 V to 0.10 V at a scan rate of 5 mVs^{-1}. The RDE rotation rates used were 100, 200, 400, 600, 900 and 1600 rpm. As in the CV experiments, the current densities are reported per mg of Pt used.

3. RESULTS AND DISCUSSION

Two types of catalysts were prepared. The first, Pt-TiO_2 (PT), lacked carbon, while the second, Pt-TiO_2-CNT (PTN), included carbon nanotubes. Figure 1 shows typical XRD patterns of the Pt-TiO_2 composites with Pt fractions of 1 *at%* (PT10), 2 *at%* (PT15) and 3 *at%* (PT20), as well as of the as-received TiO_2 (TAR) and the annealed TiO_2 nanoparticles (TAN). As shown in these figures, the main Bragg reflection at 2θ = 25.28º, associated to the TiO_2 (101) plane in the anatase structure (JPDS No. 21-1272), is observed in all samples. The other visible TiO_2 anatase reflections, (004), (200), (105), (211), (204), (220), (215) and (224), are observed at 2θ = 37.80º, 48.05º, 53.89º, 55.06º, 62.69º, 70.31º, 75.03º and 82.66º respectively, but with considerably lower intensity. The lattice parameters for the body-centered tetragonal symmetry of the TiO_2 anatase structure, calculated from the positions of the

Bragg reflections, are a = 3.787 Å and c = 9.478 Å. The XRD patterns do not exhibit the typical rutile TiO_2 reflections at 2 θ = 27.44º and 36.08º, nor the typical brookite TiO_2 structure reflections at 2 θ = 25.69º and 2 θ = 30.79º.

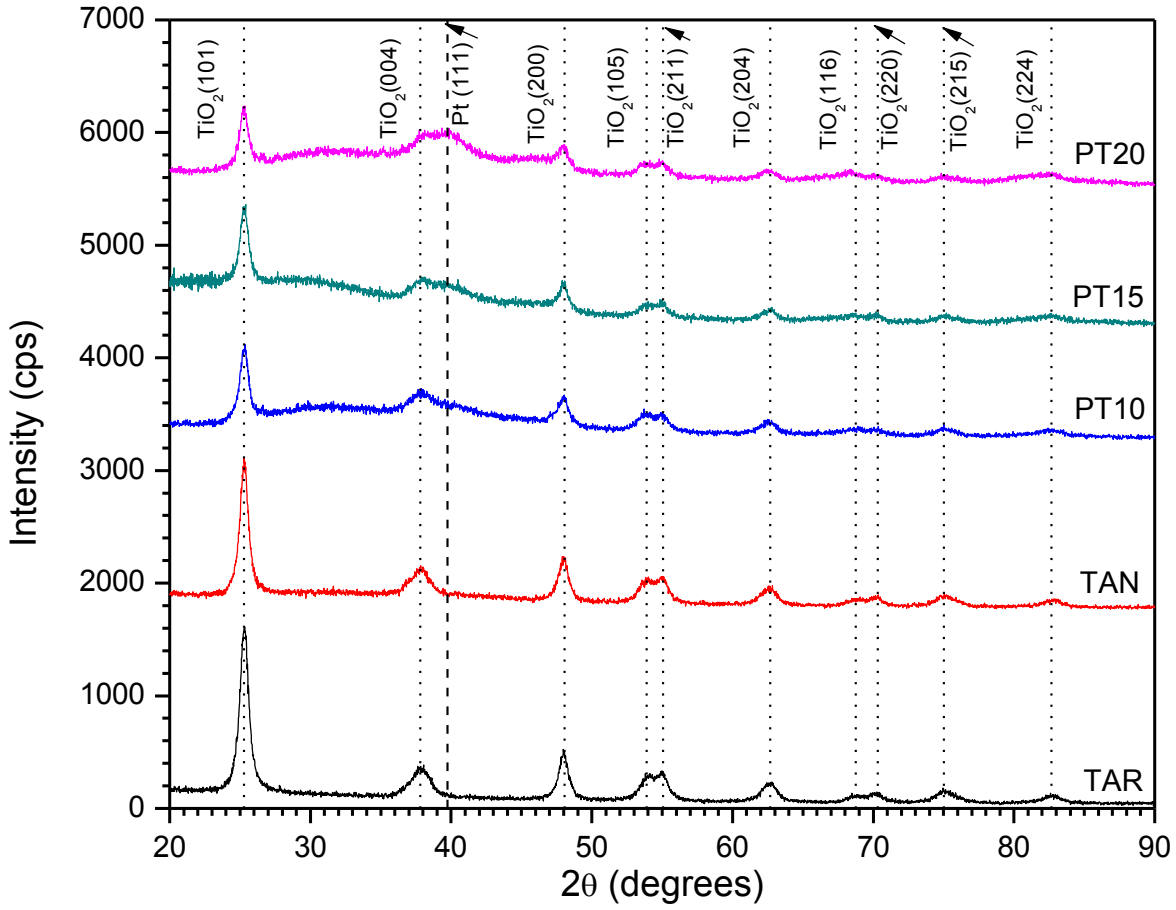

Figure 1. XRD patterns for Pt-TiO_2 composites with Pt fractions of 1 *at%* (PT10), 2 *at%* (PT15) and 3 *at%* (PT20), as well as for the as-received TiO_2 (TAR) and the annealed TiO_2 nanoparticles (TAN).

This is consistent with the lack of an anatase-to-rutile transition at temperatures below 700 ˚C [19]. Additionally, a weak Pt (111) Bragg reflection at 2 θ = 39.75º was detected for the PT20 composite, whereas only a slight shoulder, was observed for the PT10 and PT15 composites. This refection is enhanced as the Pt content of the composite is increased. Such a Pt (111) reflection is characteristic of the platinum face-centered cubic (fcc) crystal structure (JCPDS card No. 04-0802). No additional Pt (200) or Pt (220) reflections at 2 θ = 46.24º or 67.44º were detected. This result indicated that the Pt atoms were nearly fully incorporated into the TiO_2 particles. Compared to the annealed TiO_2 sample (TAN), the PT10, PT15 and PT20 composites exhibited ~50% lower TiO_2 (101) reflection intensities as a result of the Pt presence in TiO_2. The TAN sample exhibited a ~20% lower TiO_2 (101) reflection intensity than that of the as-received TAR sample.

The average particle size (d) was evaluated from the full width at half maximum of the TiO_2 (101) diffraction peak using the Debye-Scherrer Equation (1) [20].

$$d = k\lambda / (\beta \cos \theta_{max}) \quad (1)$$

In this equation, d is the average particle size (nm), λ is the wavelength of monochromatic Cu radiation (0.154 nm), θ is the Bragg angle at the peak maximum, β is the width (in radians) of the diffraction peak at a half height, and k is a coefficient ranging from 0.89-1.39 (here 0.9). The calculated 'd' value was ~11 nm for most of the investigated samples (the specific values were 11.18, 11.49, 10.54, 11.95 and 11.63 nm for TAR, TAN, PT10, PT15 and PT20 samples, respectively). Obtaining pure anatase TiO_2 in the support by the process performed in this work is important, as anatase is more catalytically active than other TiO_2 crystalline allotropes, such as rutile. The larger Ti-Ti distance and shorter Ti-O distance found in anatase indicate looser atomic packing than that observed in the rutile structure [21].

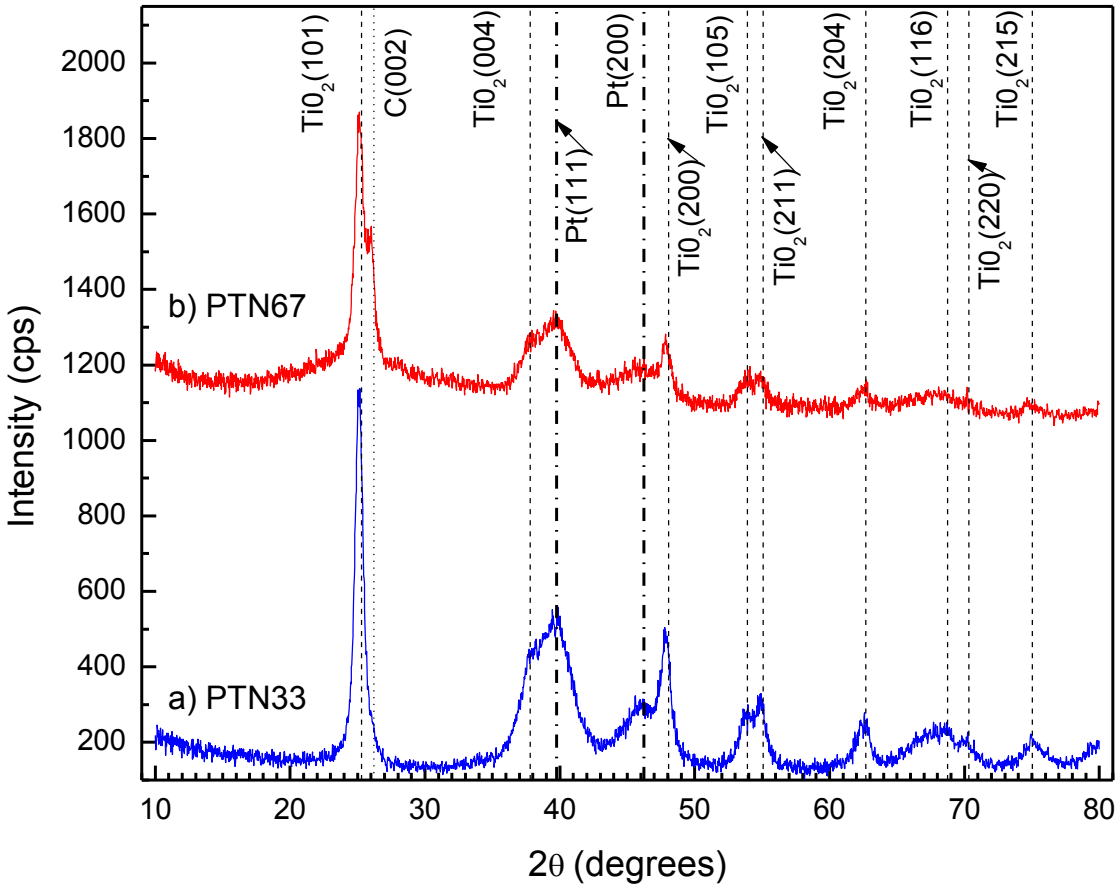

Figure 2. XRD patterns for Pt-TiO_2-CNT composites with different CNT volume fractions of (a) 33% (PTN33) and (b) 67% (PTN67).

Figure 2 shows typical XRD patterns of, (a-curve) Pt-TiO_2-33*vol%*CNT with a Pt fraction of 4 *at%* (PTN33) and (b-curve) Pt-TiO_2-67*vol%*CNT with a Pt fraction of 2 *at%* (PTN67). As shown in these figures, both composites exhibit the same main Bragg reflection at 2θ = 25.28º, assigned to the TiO_2 (101) plane in the anatase structure. The other visible TiO_2 anatase reflections, (004), (200), (105), (211), (204), (116), (220), and (215), are observed at 2 θ = 37.80º, 48.05º, 53.89º, 55.06º, 62.69º, 68.76, 70.31º, and 75.03º, respectively, but with considerably lower intensities. As mentioned previously, these reflections correspond to the body-centered tetragonal symmetry of the TiO_2 anatase structure rather than rutile TiO_2 (2 θ = 27.44º and 36.08º) or brookite TiO_2 (2 θ = 25.69º and 2 θ = 30.79º). Bragg reflections for the Pt (111), Pt (200) and Pt (220) planes at 2θ = 39.75º, 46.24º and 67.44º respectively, were detected in both samples. When Pt-TiO_2 nanotubes were synthesized by microwave irradiation [22], the composite also exhibited not only the anatase phase but also the characteristic diffraction peaks of Pt(111), Pt(200) and Pt(220) [22]. Moreover, for PTN33, the intensity and sharpness of both the TiO_2 and Pt reflection peaks were higher than for PTN67 as a result of its lower CNT content. A Bragg reflection at 2 θ = 26.22º, assigned to the (002) plane of the hexagonal graphite-2H structure of CNT, was observed for PTN67 as a result of its higher CNT content.

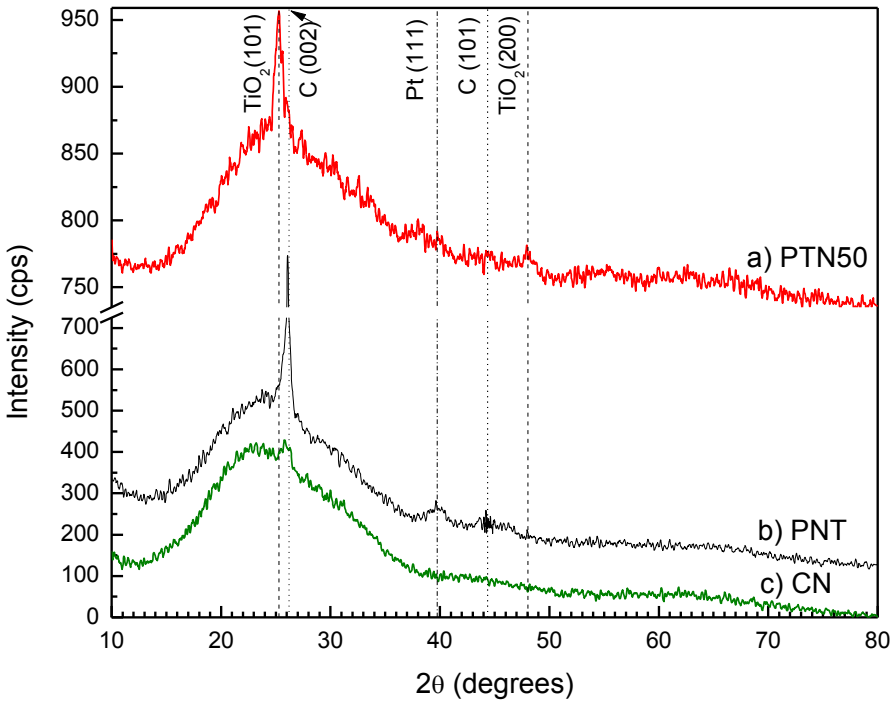

Figure 3. XRD patterns for (a) Pt-TiO_2-CNT composite with CNT fraction of 50 *vol%* (PTN50), (b) Pt-CNT composite with 99.96 *vol%* CNT (PNT) and (c) as-received CNT (CN).

Figure 3 (a-curve) shows a typical XRD pattern of Pt-TiO_2-50*vol%*CNT with a Pt fraction of 2 *at%* (PTN50). As shown in Fig. 3(a-curve), PTN50 is largely amorphous; however, crystalline TiO_2 indicated by the (101) plane of anatase is evidenced by a Bragg reflection at 2 θ = 25.28º. The TiO_2

anatase reflection (200) at 2 θ = 48.05º is only barely visible, as was the Pt (111) Bragg reflection at 2 θ = 39.75º. The predominance of amorphous materials in PTN50 is attributed to the fragmentation of the TiO_2, CNT and Pt precursor mixture performed prior to synthesis, which broke up TiO_2 agglomerates and allowed greater dispersion of Pt in this amorphous structure.

Figures 3(b and c curves) show typical XRD patterns of Pt-CNT a composite with 99.96 *vol%* CNT and a Pt fraction of 0.65 *at%* (PNT) and of the as-received CNT (CN), respectively. These figures indicate that both Pt-CNT and CNT are largely amorphous. PNT (Fig. 3(b-curve)) exhibits a crystalline hexagonal graphite-2H structure in the amorphous phase, with a main Bragg reflection at 2 θ = 26.22º assigned to the (002) plane. A very small Bragg reflection at 2 θ = 39.75º, assigned to the Pt (111) plane, was also detected for the PNT composite. The as-received CN (Fig. 3(c-curve)) exhibited an entirely amorphous diffraction pattern.

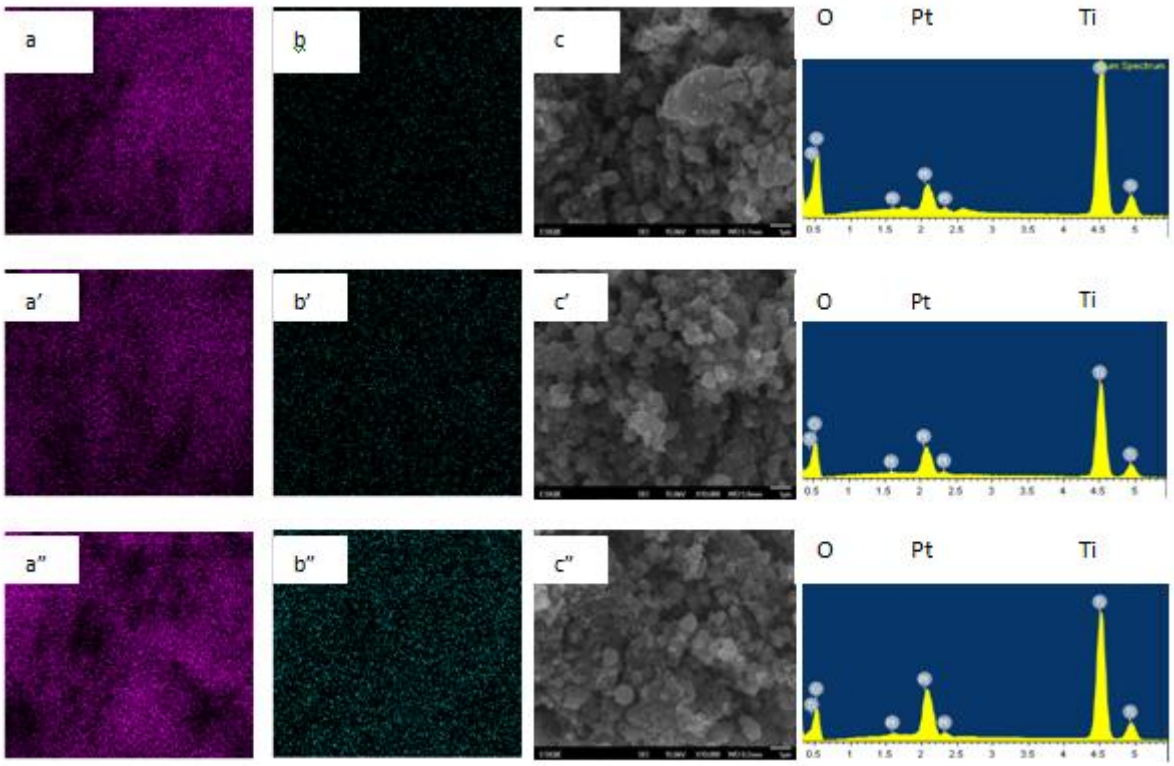

Figure 4. Element distribution maps for Ti (a-a") and Pt (b-b") as well as FESME images (c-c") and EDS spectra (right side of Figs. (c-c")) for Pt-TiO_2 composites with Pt fractions of, (a-c) 1 *at%* (PT10), (a'-c') 2 *at%* (PT15) and (a"-c") 3 *at%* (PT20).

The morphologies and particle sizes of the Pt-TiO_2 and Pt-TiO_2-CNT catalysts were studied by FESEM and STEM. Figures 4(a-c") show Ti (a-a") and Pt (b-b") element distribution maps as well as FESME images (c-c") for the Pt-TiO_2 composites, (a-c) PT10, (a'-c') PT15, and (a"-c") PT20. The corresponding EDS spectra are shown at the right side of Figs. 4(c-c"). As seen in Figures 4(c-c"), the Pt-TiO_2 composites are composed of TiO_2 agglomerates of mainly uniform particle size (0.5-1.4 μm) with a few larger agglomerates (Fig. 4(c)) (~ 3.5 μm). As shown in Figs. 4(b-b"), the Pt nanoparticles

in the three composites are uniformly deposited on the TiO_2 agglomerates. As expected, a gradual increase in the number of Pt particles number is evident as the Pt load in the composite increases: PT10 (Fig. 4(b)) < PT15 (Fig. 4 (b') < PT20 (Fig. 4 (b"). The EDS spectra of the three composites all exhibit Pt (Mα at 2.05 KeV), Ti (Kα at 4.50 KeV) and O (Kα at 0.52 KeV) lines. Quantitative chemical analyses of these elements obtained by EDS confirms the Pt content increasing from ~ 1 *at%* (Pt10) to ~ 2 *at%* (PT15) and 3 *at%* (PT20) (see Table 1).

Table 1. Elemental quantitative chemical analysis, *at%* measured by EDS

Sample	Pt	Ti	O	C
PT10	1.09	24.26	74.65	--
PT15	1.94	25.84	72.23	--
PT20	3.00	31.69	65.30	--
PTN33	4.26	17.98	43.47	34.28
PTN50	2.30	14.82	25.17	57.71
PTN67	2.18	14.09	24.42	59.32
PNT	0.65	--	--	99.34

Figures 5(a-c"') show the Ti (a-a") and Pt (b-b"') element distribution maps as well as FESME images (c-c"') for Pt-TiO_2-CNT composites, (a-c) PTN33, (a'-c') PTN50 and (a"-c") PTN67 as well as for Pt-CNT composite (b"'-c"') PNT. The corresponding EDS spectra are shown at the right side of Figs. 5(c)-(c"'). As shown in Figures 5(a, c) for PTN33 and (a", c") for PTN67, the catalysts are composed of TiO_2 particle agglomerates ranging in size from 0.5 to 1.2 μm. In these composites, the CNT are largely covered by TiO_2 and the Pt nanoparticles are uniformly deposited on such TiO_2 agglomerates. In contrast, the FESEM image of PTN50 (Fig. 5(c')) reveals several isolated CNTs in addition to the TiO_2 particle agglomerates. Ti (Fig. 5(a')) and Pt (Fig. 5(b')) exhibit more homogeneous elemental distribution in PTN50, attributable to greater disaggregation of TiO_2 and CNT's as a result of fragmentation prior to synthesis in the composite preparation. The EDS spectra of the PTN composites exhibit the presence of Pt (Mα at 2.05 KeV), Ti (Kα at 4.50 KeV), O (Kα at 0.52 KeV) and C (Kα at 0.27 KeV) lines. Quantitative chemical analyses of these elements confirms an increase in the C content from 34 *at%* (PTN33) to 59 *at%* (PTN67) along with a reduction of Pt from ~ 4 *at%* (PTN33) to ~2 *at%* (PTN67) and a reduction of Ti from ~18 *at%* (PTN33) to ~14 *at%* (PTN67) (Table 1).

PNT (Figure 5 (c’’’)) exhibits a structure of overlapping CNTs. The Pt nanoparticles deposited on these CNTs (Fig. 5(b’’’)) appear relatively dispersed due to the lack of TiO_2 support. EDS analysis of PNT exhibits only Pt and C lines, with their chemical analysis corresponding to 0.65 *at%* Pt and 99.34 *at%* C.

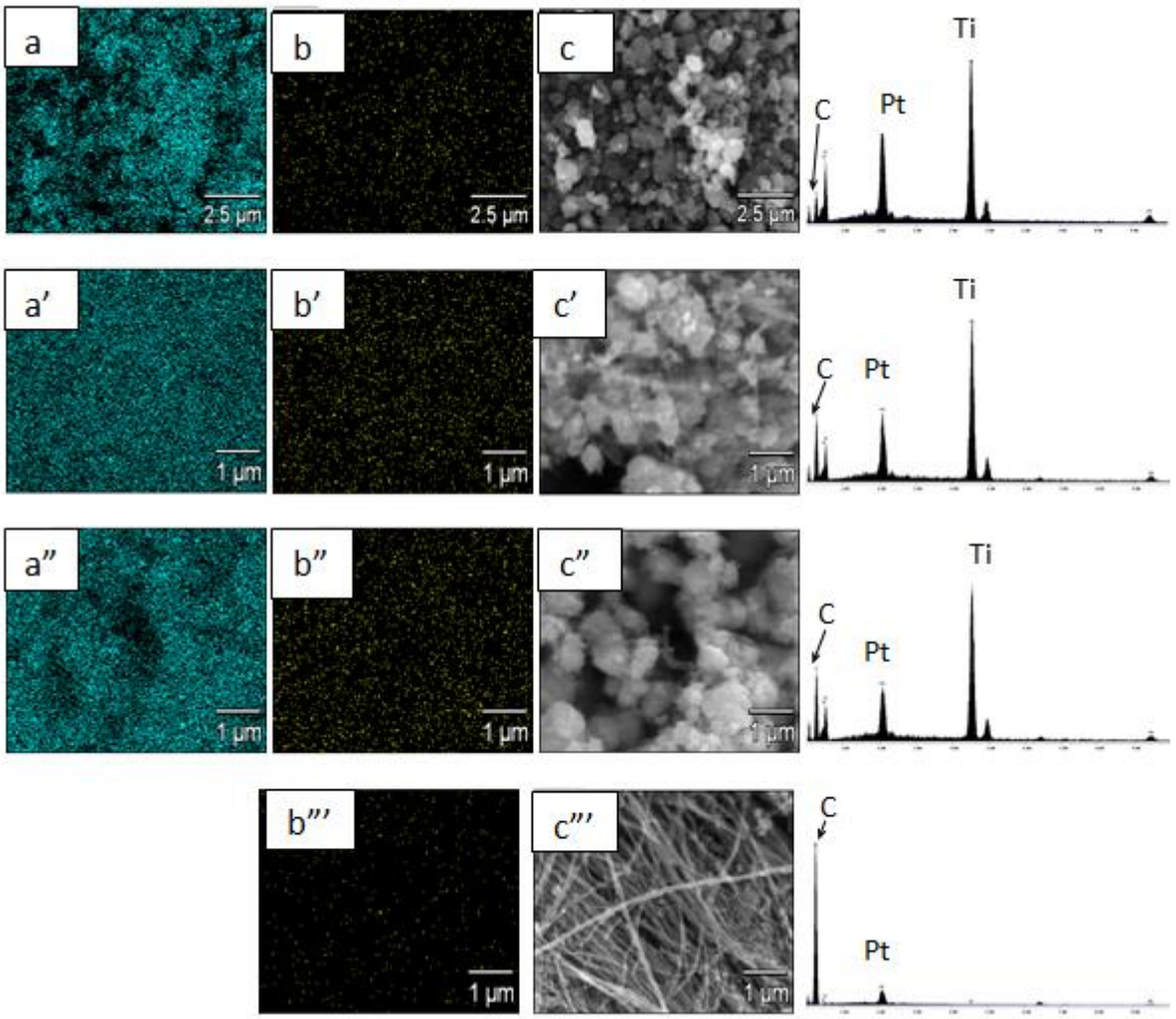

Figure 5. Element distribution maps for Ti (a-a”) and Pt (b-b’’’), as well as FESME images (c-c’’’) and EDS spectra (right side of Figs. (c-c’’’)) for Pt-TiO_2-CNT composites with CNT fractions of, (a-c) 33 *vol%* (PTN33), (a’-c’) 50 *vol%* (PTN50) and (a”-c”) 67 *vol%* (PTN67), along with Pt-CNT composite (b’’’-c’’’) with CNT fraction of 99.96 *vol%* (PNT).

Figures 6(a-d) show STEM images of typical CNTs found in the PTN33 (a), PTN50 (b), PTN67 (c) and PNT (d) composites. These figures show Pt nanoparticles (size 3-5 nm) deposited on the CNT surfaces (CNT diameter, 50-90 nm). Fig. 6(a) also shows Pt nanoparticles deposited on TiO_2 agglomerates. The PNT (Fig. 6(d)) and PTN50 composites (Fig. 6(b)) exhibit a larger number of isolated CNTs than PTN33 (Fig. 6(a)).

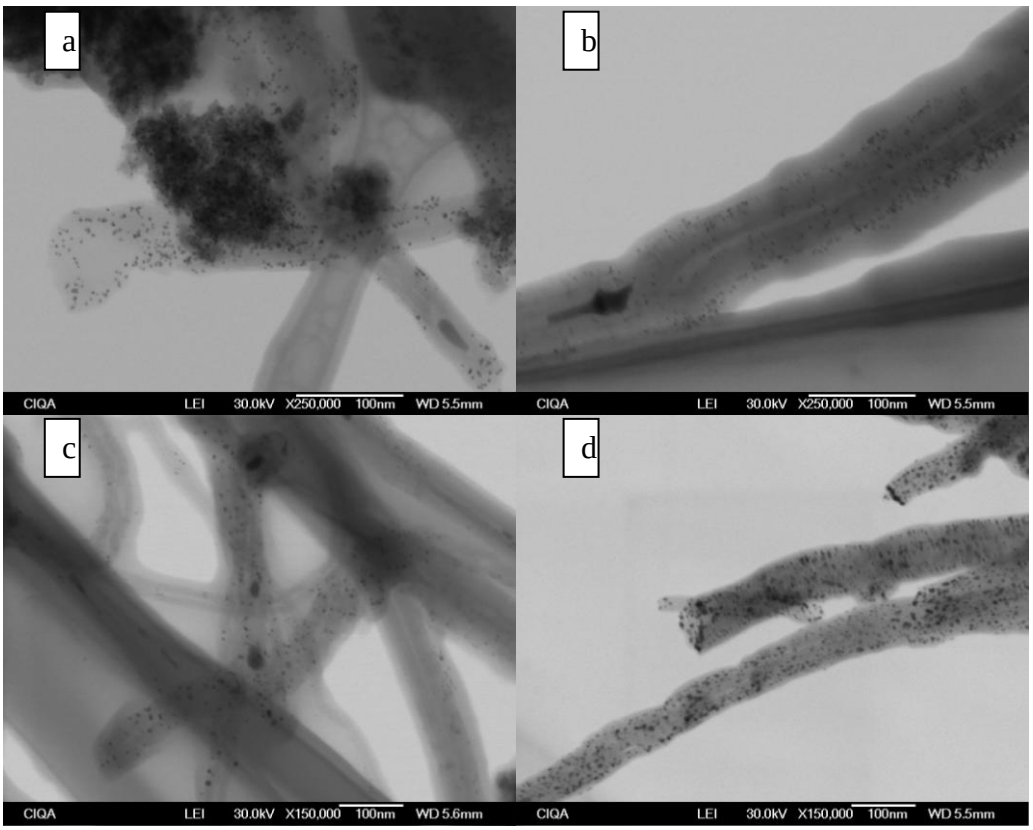

Figure 6. STEM images of typical Pt-CNTs found in (a) PTN33, (b) PTN50, (c) PTN67 and (d) PNT composites.

Cyclic voltammograms (CV) for the Pt-TiO_2-based cathodes PT10, PT15 and PT20 are presented in Figures 7(a-c) respectively. These CVs were recorded over a potential range from -0.1 to 1.28 V at a scan rate of 50 mVs^{-1} over 1 to 50 cycles in an N_2-saturated 0.5 M H_2SO_4 electrolyte. The current densities are reported per mg of Pt. As shown in Figures 7(a-c), in the absence of CNTs, there is no characteristic hydrogen adsorption/desorption region in the first CV cycle. Nevertheless, in the 25th and 50th cycles, a weak hydrogen desorption peak (~ 5 mA $(mg\ Pt)^{-1}$) is detected at 0.074 V for PT15 and at 0.096 V for PT20. All of the TiO_2-supported Pt composites exhibited good stability, which was confirmed by the consistency of the CV pattern after 25 and 50 cycles.

Figures 8(a-b) present cyclic voltammograms for the Pt-TiO_2-CNT composites, (a) PTN33 and (b) PTN67. As shown in these figures, hydrogen adsorption/desorption, which is characteristic of polycrystalline platinum electrodes, was considerably more evident in PTN33 and PTN67 than for the PT composites. The hydrogen desorption peak for the PTN composites is well defined with much higher current densities (17 - 62 mA $(mg\ Pt)^{-1}$) than that exhibited by PT15 or PT20. Additionally, the first CV cycle of PTN67 reveals a slight oxide formation peak at 0.790 V that is not detected in the CV of PT composites. This peak is attributed to the formation of Pt-O, which generally occurs at a potential of 0.800 V ($Pt + H_2O \leftrightarrow Pt\text{-}O + 2H^+ + 2e^-$). The reduction of Pt-O was not clearly detected.

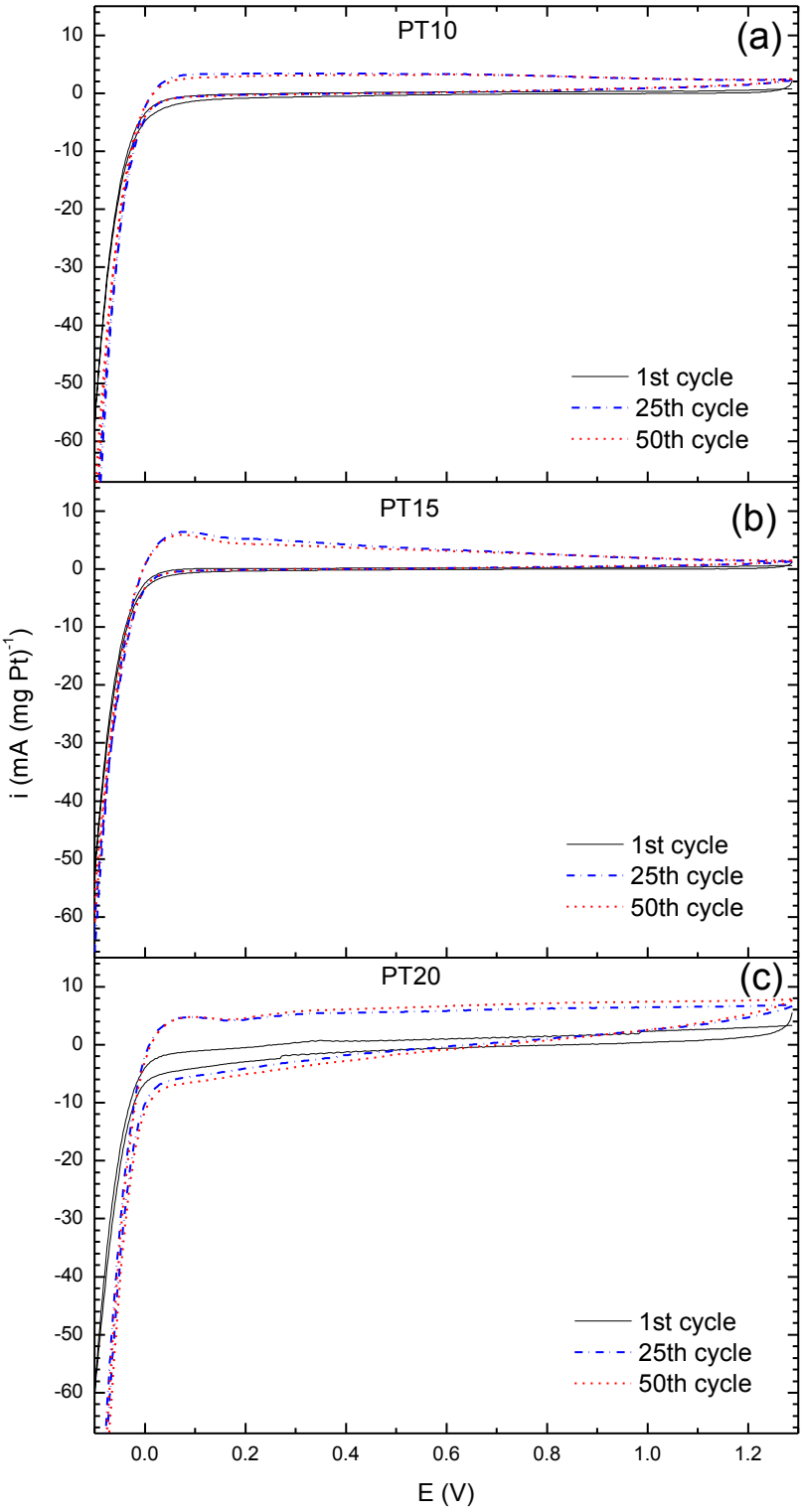

Figure 7. Cyclic voltammograms for Pt-TiO_2 composites with Pt fractions of (a) 1 *at%* (PT10), (b) 2*at%* (PT15) and (c) 3*at%* (PT20), at scan rate of 50 mVs^{-1}, in N_2 saturated 0.5 M H_2SO_4 solution.

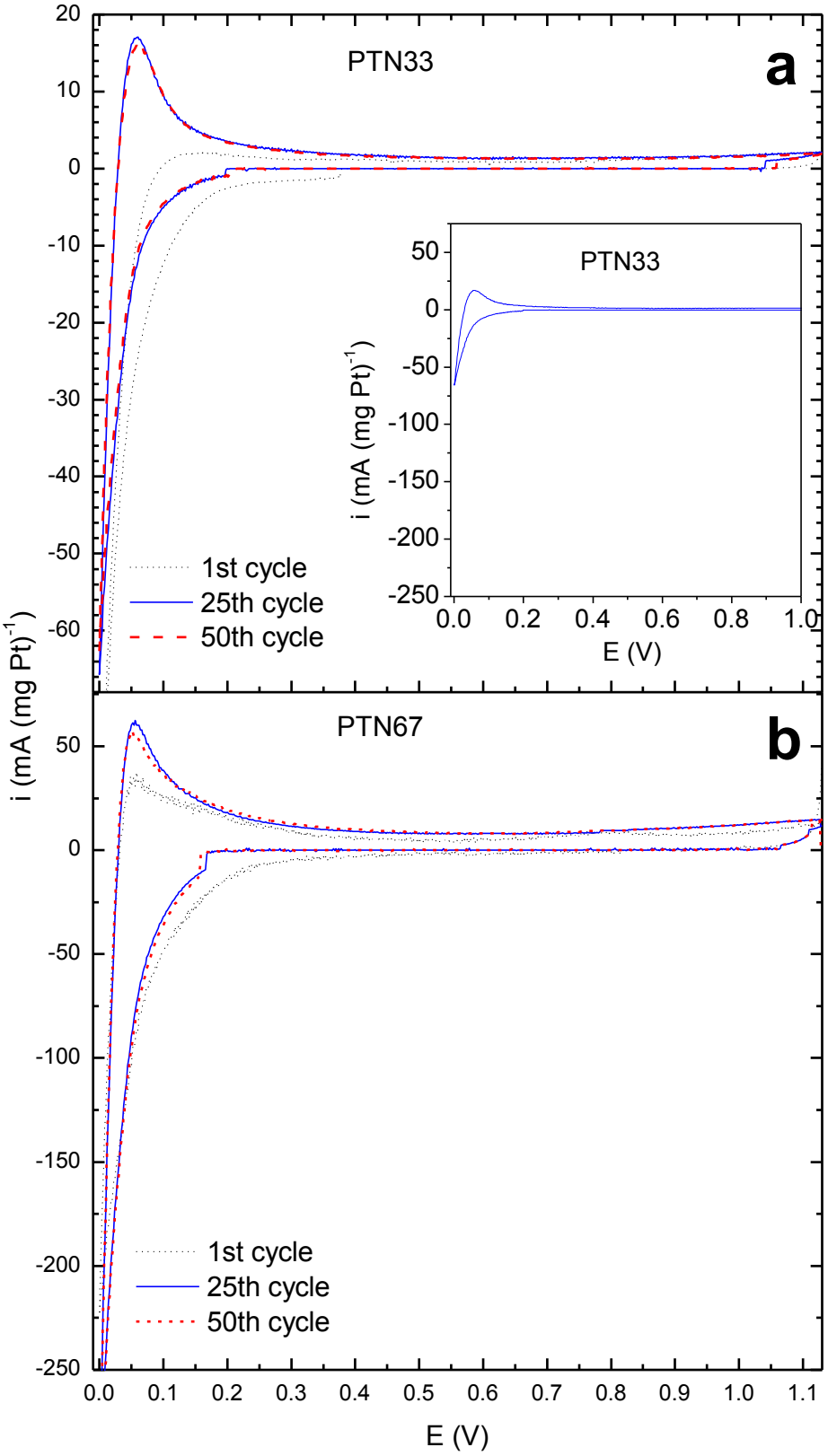

Figure 8. Cyclic voltammetry curves for Pt-TiO_2-CNT composites with different CNT volume fractions of, (a) 33% (PTN33) and (b) 67% (PTN67) in N_2-saturated 0.5 M H_2SO_4 solution at scan rate of 50 mVs^{-1}. The inset in (a) shows the PTN33 CVs at the same current density scale than those of PTN67.

Figs. 8(a-b) also show that the current density of the hydrogen desorption peak exhibited by PTN67 on the 25th cycle (~ 62 mA (mg Pt)$^{-1}$) at ~ 0.060 V was more than three times higher than that of PTN33 (~ 17 mA (mg Pt)$^{-1}$), despite the fact that PTN67 has half the Pt *at%* and twice the CNT *at%* of PTN33.

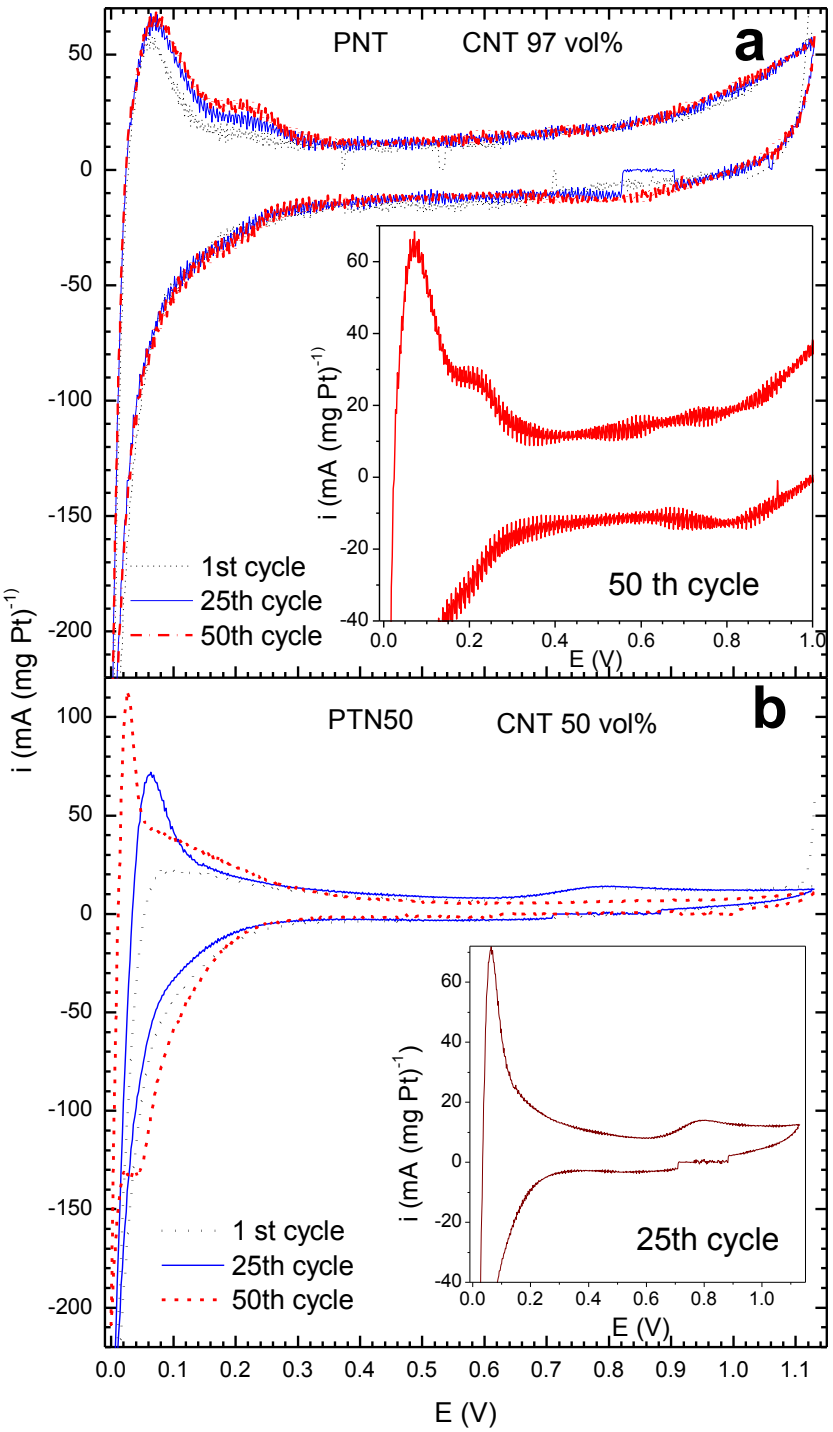

Figure 9. Cyclic voltammograms for (a) Pt-CNT (PNT) catalyst and for (b) Pt-TiO_2-CNT composite, with 50 *vol%* CNT (PTN50), at scan rate of 50 mVs^{-1}, in N_2 saturated 0.5 M H_2SO_4 solution. The insets show details of CVs cycles, in (a) 50th cycle for PNT and in (b) 25th cycle for PTN50 composites.

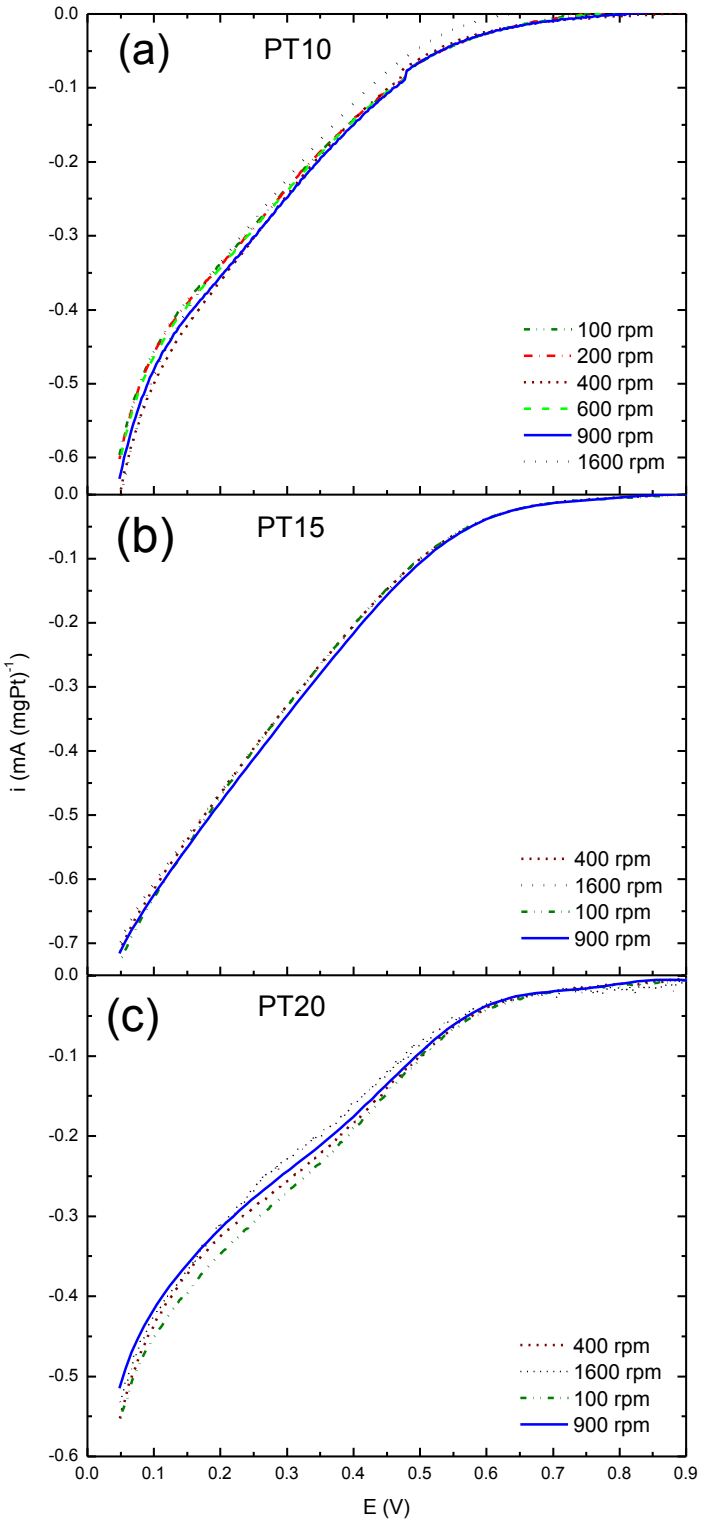

Figure 10. ORR Polarization curves for Pt-TiO_2 catalysts with Pt fractions of (a) 1 at% (PT10), (b) 2 *at%* (PT15) and (c) 3 *at%* (PT20) in O_2-saturated 0.5 M H_2SO_4 at scan rate of 5 mVs^{-1} and different electrode rotation rates between 100 and 1600 rpm.

The use of CNTs as electrical conductors for Pt nanoparticles explains this observation. Consequently, the current density increases exhibited by PTN67, in comparison to PTN33 (and also with respect to PT composites), is not caused by an increase in the catalytic area of the Pt nanoparticles but by the addition of conductive CNTs. The increase in the hydrogen desorption peak also reflects the efficiency of Pt utilization.

As shown in Figures 7 and 8, the states of the Pt-TiO_2 and Pt-TiO_2-CNT composite electrodes over 50 cycles were relatively similar to those exhibited after 25 cycles. This observation is indicative of a negligible loss of the active Pt surface due to extended cycling and confirms the catalyst stability provided by the TiO_2 support.

Figures 9(a-b) show cyclic voltammograms of a Pt-TiO_2-CNT composite, PTN50 (b) and a Pt-CNT composite PNT (a), which is presented as reference. As shown in these figures, both PNT and PTN50 exhibit hydrogen adsorption/desorption current densities that are greater than those of PTN33 and PTN67. As shown in the inset of Fig. 9(a), the CV profiles of PNT exhibit hydrogen desorption peaks at 0.072 V and 0.208 V. The PTN50 composite (50th cycle) exhibits hydrogen adsorption/desorption peaks at 0.030 V (Fig. 9(b)). However, the current density of the hydrogen desorption peak for PTN50 (113.50 mA (mg Pt)$^{-1}$) is higher than that exhibited by PNT (62.45 mA (mg Pt)$^{-1}$). On the 25th cycle, the current density of the hydrogen desorption peak (at 0.064 V) for PTN50 (71 mA (mg Pt)$^{-1}$) is comparable to that of PNT (68 mA (mg Pt)$^{-1}$). A subtle platinum oxide formation peak is also visible at 0.798 V in the anodic potential cycle for PTN50 in both the first and the 25th cycles (inset of Fig. 9(b)). PTN50 exhibits better catalytic activity than PTN33 and PTN67, which is attributed to its small, highly dispersed Pt nanocrystals (despite its lower *vol%* of CNT compared to PTN67). Such catalytic activity is the result of the greater fragmentation of CNTs, Pt and TiO_2 employed prior to the synthesis of PTN50 as opposed to the synthesis procedures for PTN33 and PTN67.

Comparing the electrocatalytical activities of Pt-TiO_2-CNT catalysts synthesized by a different route [23] with those obtained in this work, it is clear that with our synthesis route is possible to obtain Pt-TiO_2-CNT catalysts for ORR with good activity.

Figures 10(a-c) show the ORR current density–potential (*i*-E) curves for the Pt-TiO_2 catalysts, (a) PT10, (b) PT15 and (c) PT20. The *i*-E curves for the three composites are characterized by an electron transfer kinetics pattern: a lower activation overpotential is required as the Pt content is increased. PT20 exhibits a weak mixed electron transfer - mass transfer region at negative potentials (of 0.400 V); however, it does not present a flat plateau in the oxygen diffusion controlled region. The absence of the three characteristic control zones for ORR implies that Pt-TiO_2 has poor catalytic activity, likely due to the low conductivity of TiO_2.

Figures 11(a-c) show the ORR current density–potential curves for the Pt-TiO_2-CNT composites, PTN33, PTN50 and PTN67, respectively. The measured OCP values were 0.952 V, 0.954 V and 0.968 V and the overpotentials, with respect to the reversible ORR potential, were 0.274 V, 0.272 V and 0.258 V for PTN33, PTN50 and PTN67, respectively. As shown in Fig. 11(a), the ORR process for PTN33 is controlled by electron transfer at low overpotentials (0.952 V to 0.680 V) where the current density is independent of the electrode rotation rate. A variation of the current density with the electrode rotation rate is observed at higher overpotentials (0.680 to 0.100 V). The absence of a

horizontal plateau for PTN33 indicates that while the process is controlled by oxygen diffusion to the electrode surface, the electron transfer contributes significantly to the current, resulting in a mixed control.

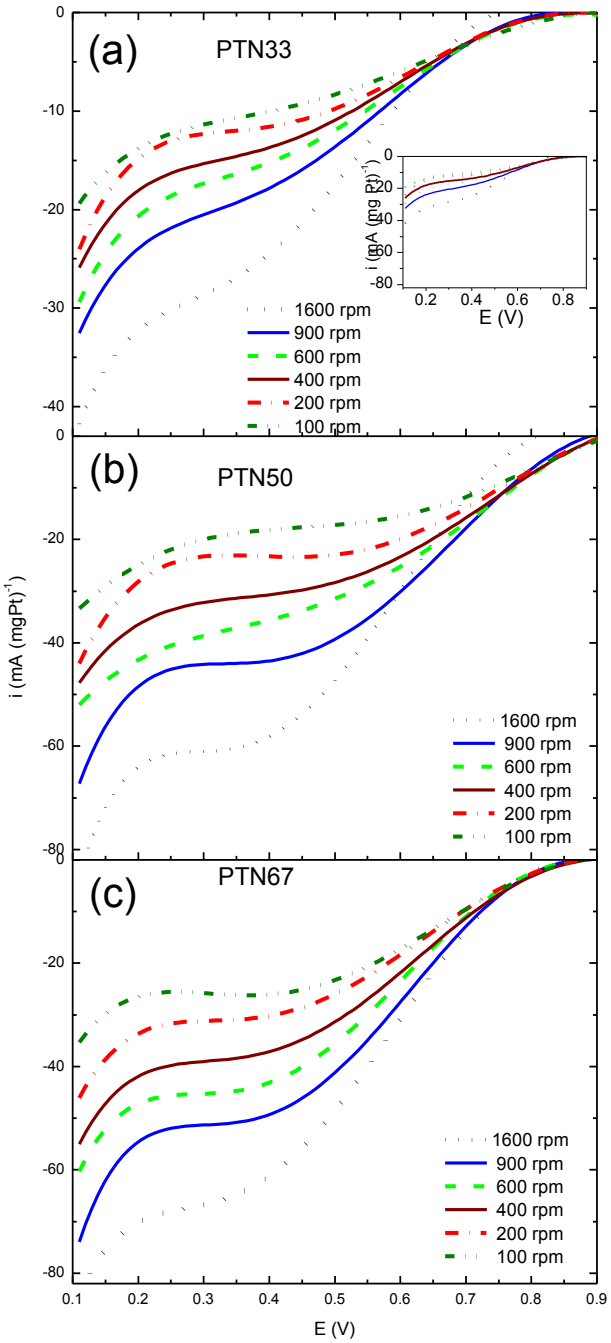

Figure 11. ORR polarization curves for Pt-TiO_2-CNT catalysts with different CNT volume fractions of (a) 33% (PTN33), (b) 50% (PTN50) and (c) 67% (PTN67) in O_2-saturated 0.5 M H_2SO_4 at scan rate of 5 mVs^{-1} and at several electrode rotation rates, 100 - 1600 rpm. The inset in (a) shows the PTN33 *i*-E curves at the same current density scale than those of PTN50 and PTN67.

For PTN50 and PTN67 (Figs. 11(b and c)), the *i*-E curves exhibit three typical regions related to an electron transfer region, a mixed electron transfer - mass transfer region, and purely mass transfer region. The process is controlled by electron transfer at low overpotentials, from 0.954 V to 0.785 V and from 0.968 V to 0.775 V for PTN50 and PTN67, respectively. Mixed control is evident at higher overpotentials, from 0.785 V to 0.570 V for PTN50 and from 0.775 V to 0.450 V for PTN67 (measured at 200 rpm). A limiting steady-state current density, which increases with the electrode rotation rate, is established by oxygen diffusion to the electrode surface at still higher overpotentials, from 0.570 V to 0.200 V and from 0.450 V to 0.200 V for PTN50 and PTN67, respectively.

The PTN50 and PTN67 *i*-E curves (Figs. 11(b and c)) exhibited significant differences with those of PTN33 (Fig. 11(a)). PTN50 and PTN67 exhibit more ORR catalytically active sites than PTN33. The three process control zones are better defined and the current densities are larger for PTN50 and PTN67 than for PTN33. For PTN50 and PTN67, the electron-transfer overpotentials (0.170 V and 0.193 V, respectively) are smaller than for PTN33 (0.277 V), and the limiting steady-state current densities are attained quicker at lower overpotentials than for PTN33. Additionally, the steady-state limit current measurements for PTN50 and PTN67 are performed with higher precision than for PTN33 due to the negligible contributions of electron-transfer kinetics to mass transfer. These factors denote that the PTN50 and PTN67 composites, with higher *vol%* CNT, have better catalytic activities towards ORR than PTN33, attributable to their better electrical conductivities. Moreover, PTN50 exhibits a larger steady state current density gap (0.370 V) than PTN67 (0.250 V) due to its enhanced catalytic activity resulting from its small, highly dispersed Pt nanocrystals (despite its lower *vol%* CNT compared to PTN67). The enhanced activity may be explained by the greater fragmentation of CNT along with Pt and TiO_2 particles prior to the synthesis of PTN50, which was not performed in the syntheses of PTN33 and PTN67. This technique prevents the agglomeration of platinum particles. This explanation is supported by the XRD analysis of PTN50, which shows Pt dispersed on a vitreous phase composed of TiO_2 and CNT (Fig. 3 (a-curve)). This largely amorphous material reacts more quickly than materials where the Pt is present on crystalline phases (TiO_2 and CNT) as in PTN67 (Fig. 2(a-curve)).

Comparing the overpotentials of Pt-TiO_2-C synthesized by a different route [24] with those obtained in this work, it is observable that with our synthesis route is possible to obtain Pt-TiO_2-CNT catalysts for ORR with minor overpotentials.

Figure 12 shows the ORR *i*-E curves for the PNT composite containing 99.96 *vol%* CNT. In this composite, the raw materials were fragmented prior to synthesis. As shown in this figure, the *i*-E curves exhibit three typical regions, related to an electron transfer region, a mixed electron transfer - mass transfer region, and purely mass transfer region. The measured OCP value was 1.007 V, and the overpotential with respect to the reversible ORR potential was 0.219 V. At low overpotentials (0.135 V), the process is controlled by electron transfer. At higher overpotentials (0.872 to 0.500 V), the process is controlled by both the oxygen diffusion to the electrode surface and by the electron transfer. At these overpotentials, the current density increases with the electrode rotation rate. At even higher overpotentials (0.500 to 0.200 V), the process is controlled by the oxygen diffusion to the electrode surface, and here a limiting steady state current density is established. The current density values exhibited by the *i*-E curves of the PNT composite (Fig. 12) were higher than those found for PTN

composites (Fig. 11), indicating that PNT has better catalytic activity towards ORR than PTN catalysts. There is likely a greater surface availability for Pt particles deposited on CNT than those deposited on TiO_2-CNT. Such greater surface availability favors the adsorption of the oxygen on their surface and increases the charge transfer between platinum and oxygen molecules.

As mentioned previously, the O_2 reduction currents measured for the Pt-TiO_2 composites alone were low due to the low electronic conductivity in bulk TiO_2. However, the Pt-TiO_2-CNT composite cathodes showed enhanced cathode performance, which increased with increasing CNT fraction. At 0.8 V and 400 rpm, the current densities for Pt-TiO_2-CNT composites were measured to be in the order of PTN50 (5.40 mA (mg Pt)$^{-1}$) > PTN67 (2.11 mA (mg Pt)$^{-1}$) > PTN33 (1.06 mA (mg Pt)$^{-1}$). Nevertheless, the direct deposition of Pt on CNT still provides the best electrocatalytic activity (PNT, 60.83 mA (mg Pt)$^{-1}$).

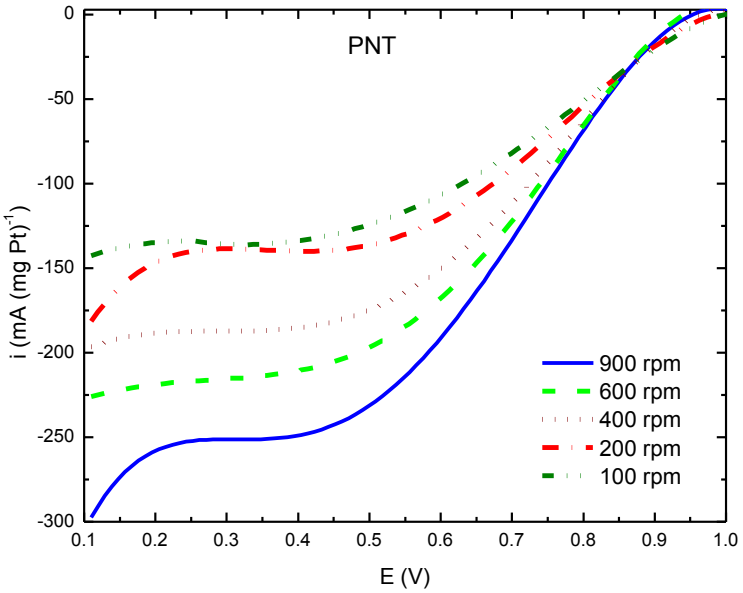

Figure 12. ORR polarization curves for Pt-CNT catalyst with 0.65 *at%* of Pt (PNT) in O_2-saturated 0.5 M H_2SO_4 at scan rate of 5 mVs^{-1} and at different electrode rotation rates, 100 - 900 rpm.

If we compare the electrocatalytical activities of Pt-C, Pt-TiO_2 and Pt-TiO_2-CNT synthesized by different routes [14, 17, 22-27] with those obtained in this work, it is clear that with our synthesis route is possible to obtain Pt-TiO_2-CNT catalysts for ORR with a good activity and minor overpotential using lower platinum loadings. A mix of TiO_2-CNT rich in CNT is promising alternative as electrocatalyst support for HER.

4. CONCLUSIONS

TiO_2 anatase (body-centered tetragonal structure) was the main crystalline phase present after the synthesis of the Pt-TiO_2 and Pt-TiO_2-CNT composites, which was confirmed by XRD. However, when fragmentation of the raw material was vigorous, the particle size became smaller and the

resulting Pt-TiO_2-CNT composites displayed an amorphous structure. STEM micrographs of the composites showed well-dispersed Pt nanoparticles deposited on anatase TiO_2 agglomerates and on CNTs.

Increased amounts of Pt deposited on TiO_2 enhanced the electrochemical activity of the cathode in the order PT10 < PT15 < PT20. In these PT composites, the Pt particles on TiO_2 aggregates are isolated for electron transport, indicating that the electrodes are limited by insufficient local electronic conductivity because of the low bulk electronic conductivity of TiO_2. In contrast, the macroscopic electronic conductivities of Pt-TiO_2-CNT composite electrodes are higher than that of the Pt-TiO_2 catalysts due to the creation of electron-conducting CNT networks in the electrode. Accordingly, the Pt utilization is higher in Pt-TiO_2-CNT catalysts than in Pt-TiO_2 composite electrodes. The increase in the CV hydrogen desorption peak area illustrates improved Pt utilization when the fraction of electron-conducting component increased. As a result, Pt utilization is higher for PTN67 than for PTN33. The CV results showed that the activity of 'aged' CNT and metal oxide-supported catalysts subjected to extended voltammetric cycling was maintained.

The CNT-supported catalyst yielded the best performance in ORR because of its higher Pt activity resulting from the relatively high conductivity of the CNT support. The carbon-free Pt-TiO_2 cathode had, in contrast, an expected lower oxygen reduction activity due to the limited macroscopic electronic conductivity of TiO_2. The catalytic activity towards ORR is very sensitive to the electrical conductivity of the Pt-TiO_2-CNT composites and improves significantly when the CNT percentage (conductive phase) increases. For instance, the Pt-TiO_2-CNT catalysts with 50 *vol%* CNT and 67 *vol%* CNT exhibited higher catalytic performance than that found with 33 *vol%* CNT because of the significant increase in the direct Pt-CNT contact. Additionally, the catalytic activity towards ORR is very sensitive to raw material fragmentation. When this process is more vigorous, the particle size becomes smaller and the resulting Pt-TiO_2-CNT composites display better Pt activity. For instance, PTN50 (for which raw materials were more fragmented) exhibited higher Pt activity than Pt-TiO_2-CNT composites without vigorous fragmentation (PTN33 and PTN67), irrespective of the higher CNT percentage (PTN67). The performances of PTN50 and PTN67 towards ORR were only slightly lower than that found for the Pt-CNT cathode.

ACKNOWLEDGMENTS
Funding from the National Science and Technology Council of Mexico (CONACYT), under 60047 project is gratefully acknowledged.

References

1. S. V. Kraemer, K. Wikander, G. Lindbergh, A. Lundblad and A.E.C. Palmqvist, *J. Power Sources*, 180 (2008) 185.
2. K. W. Park and K. S. Seol, *Electrochem. Commun.* 9 (2007) 2256.
3. X. Wang, W. Li, Z. Chen, M. Waje and Y. Yan, *J. Power Sources* 158 (2006) 154.
4. B.Y. Xia, H. B. Wu, J. S. Chen, Z. Wang, X. Wang and X. W. Lou. *Phys. Chem. Chem. Phys.*, 14 (2012) 473.
5. Y-W. Lee, D-H. Kwak, A-R. Park, B. Roh, I. Hwang, G. Cao and K-W Park, *Int. J. Electrochem. Sci.*, 8 (2013) 9499.

6. E. Antolini and E. R. Gonzalez, *Solid State Ionics* 180, 9-10 (2009) 746.
7. R. Phillips, A. O'Toole, X. He, R. Hansen, R. Geer, and E. Eisenbraun, *J. Mater. Res.*, 28, 3 (2013) 461.
8. L. Chevallier, A. Bauer, S. Cavaliere, R. Hui, J. Rozière and D. J. Jones, *ACS Appl. Mater. Interfaces* 4, 3 (2012) 1752.
9. K. Senevirathne, R. Hui, S. Campbell, S. Ye and J. Zhang, *Electrochim. Acta* 59 (2012) 538.
10. B. Y. Xia, S. Ding, H. B. Wu, X. Wang and X. Wen, *RSC Advances*, 2 (2012) 792.
11. H. Huang, D. Y. C. Leung, and D. Yeb, *J. Mater. Chem.*, 21 (2011) 9647.
12. X. Li, C. Liu, W. Xing and T. Lu, *J. Power Sources* 193 (2009) 470.
13. D. Wen, S. Guo, J. Zhai, L. Deng, W. Ren and S. Dong, *J. Phys. Chem. C* 113 (2009) 13023.
14. N. Rajalakshmi, N. Lakshmi and K.S. Dhathathreyan, *Int. J. Hydrogen Energy* 33 (2008) 7521.
15. S. Cavaliere, S. Subianto, I. Savych, D. J. Jones and J. Rozière, Energy & Environ. Sc. 4 (2011) 4761.
16. A. Bauer, K. Lee, C. Song, Y. Xie, J. Zhang and R. Hui, *J. Power Sources* 195 (2010) 3105.
17. W. J. Lee, M. Alhosan, S.L. Yohe, N.L. Macy and W.H. Smyrl, *J. Electrochem. Soc.* 155, 9 (2008) B915.
18. S.Y. Huang, P. Ganesan, S. Park and B.N. Popov, *J. Am. Chem. Soc.* 131(2009) 13898.
19. C. Perego, R. Revel, O. Durupthy, S. Cassaignon and J. P. Jolivet, Solid State Sci. 12 (2010) 989.
20. Z.B. Wang, G.P. Yin, J. Zhang, Y.C. Sun and P.F. Shi, *Electrochim. Acta* 51 (2006) 5691.
21. L. Vayssieres, *On Solar Hydrogen & Nanotechnology*, John Wiley & Sons, Chi., UK (2010).
22. Q. Long, M. Cai, J. Li, H. Rong and L. Jiang, *J. Nanopart. Res.* 13 (2011) 1655.
23. K. Huang, K. Sasaki, R.R. Adzic and Y. Xing, *J. Mater. Chem.*, 22 (2012) 16824.
24. X. Liu, J. Chen, G. Liu, L. Zhang, H. Zhang and B. Yi, *J. Power Sources* 195 (2010) 4098.
25. D.Y. Kim, S.B. Han, Y.W. Lee and K.W. Park, *Mater. Chem. Phys.* 137 (2013) 704.
26. Y. Fan, Z. Yang, P. Huang, X. Zhang and Y.M. Liu, *Electrochim. Acta* 105 (2013) 157.
27. W.J. Lee, D.H. Lim and W.H. Smyrl, *J. Power Sources* 240 (2013) 612.